

Article

# Promotion of the Efficient Electrocatalytic Production of H<sub>2</sub>O<sub>2</sub> by N,O- Co-Doped Porous Carbon

Lina Sun <sup>1,2</sup>, Liping Sun <sup>1</sup>, Lihua Huo <sup>1</sup> and Hui Zhao <sup>1,\*</sup> 

<sup>1</sup> Key Laboratory of Functional Inorganic Material Chemistry, Ministry of Education, School of Chemistry and Materials Science, Heilongjiang University, Harbin 150080, China

<sup>2</sup> Key Laboratory of Molten Salts and Functional Materials of Heilongjiang Province, School of Science, Heihe University, Heihe 164300, China

\* Correspondence: zhaohui98@hlju.edu.cn

**Abstract:** H<sub>2</sub>O<sub>2</sub> generation via an electrochemical two-electron oxygen reduction (2e<sup>-</sup> ORR) is a potential candidate to replace the industrial anthraquinone process. In this study, porous carbon catalysts co-doped by nitrogen and oxygen are successfully synthesized by the pyrolysis and oxidation of a ZIF-67 precursor. The catalyst exhibits a selectivity of ~83.1% for 2e<sup>-</sup> ORR, with the electron-transferring number approaching 2.33, and generation rate of 2909.79 mmol g<sup>-1</sup> h<sup>-1</sup> at 0.36 V (vs. RHE) in KOH solution (0.1 M). The results prove that graphitic N and -COOH functional groups act as the catalytic centers for this reaction, and the two functional groups work together to greatly enhance the performance of 2e<sup>-</sup> ORR. In addition, the introduction of the -COOH functional group increases the hydrophilicity and the zeta potential of the carbon materials, which also promotes the 2e<sup>-</sup> ORR. The study provides a new understanding of the production of H<sub>2</sub>O<sub>2</sub> by electrocatalytic oxygen reduction with MOF-derived carbon catalysts.

**Keywords:** porous carbon; two-electron reduction of oxygen; hydrogen peroxide; electrocatalyst



**Citation:** Sun, L.; Sun, L.; Huo, L.; Zhao, H. Promotion of the Efficient Electrocatalytic Production of H<sub>2</sub>O<sub>2</sub> by N,O- Co-Doped Porous Carbon. *Nanomaterials* **2023**, *13*, 1188. <https://doi.org/10.3390/nano13071188>

Academic Editor: Adriano Sacco

Received: 21 February 2023

Revised: 18 March 2023

Accepted: 22 March 2023

Published: 27 March 2023



**Copyright:** © 2023 by the authors. Licensee MDPI, Basel, Switzerland. This article is an open access article distributed under the terms and conditions of the Creative Commons Attribution (CC BY) license (<https://creativecommons.org/licenses/by/4.0/>).

## 1. Introduction

Hydrogen peroxide (H<sub>2</sub>O<sub>2</sub>) is regarded as one of the most significant chemical compounds [1–3]. It serves as both a desirable energy carrier and a green oxidant and disinfectant. It is comprehensively applied in the industries of medicine and environmental protection, such as the bleach of paper pulp and textiles [4–6]. To date, the majority of the industrial processes for producing H<sub>2</sub>O<sub>2</sub> depend on the process of anthraquinone oxidation. This is a complex and energy-intensive procedure, with a large quantity output of chemical waste [7–9]. Since Beal first reported the electrochemical production of H<sub>2</sub>O<sub>2</sub> in the 1930s [10], the electrochemical reduction of oxygen has been gradually realized as a potential approach for the generation of H<sub>2</sub>O<sub>2</sub> [11–14].

In order to produce H<sub>2</sub>O<sub>2</sub> in an electrochemical way, it is crucial to explore novel electrocatalysts with superior activity, selectivity, stability and low cost [11]. Compared to noble metals and alloys (Pt-Hg [13], Pd-Au [15] and Pd-Hg [16]), carbon materials were extensively explored for their good abundance, low cost and easy functionalization [17–23]. The electronic structure of carbons is regulatable by some dopants such as heteroatoms [24,25], and the heteroatoms themselves can also act as active centers for ORR [26–28], thereby improving the catalytic activity. Particularly, it is of importance to dope nitrogen (N) in facilitating the oxygen reduction reaction through two electrons (2e<sup>-</sup> ORR) for H<sub>2</sub>O<sub>2</sub> production [29–32]. It is widely accepted that the doping of nitrogen into the carbon materials can drastically lower the overpotential of 2e<sup>-</sup> ORR by the reduction in the Gibbs free-energy of O<sub>2</sub> reduction and the optimization of the binding energy of HOO<sup>-</sup> [31,33]. In alternative studies, the electrocatalytic activity of oxygen-substituted carbon materials is investigated. Xia et al. [34] explored a convenient approach to oxidize commercial carbon blacks with concentrated nitric acid. Oxygen functional groups were

then introduced as active sites to increase the  $\text{H}_2\text{O}_2$  selectivity up to ~95%. Recently, carbon materials with two kinds of active centers in the framework were prepared to further promote the catalytic property for  $\text{H}_2\text{O}_2$  electroproduction. For example, Zhao [35] et al. prepared the COOH-terminated N-doping carbon aerogel. The production rate for  $\text{H}_2\text{O}_2$  was as high as  $0.071 \text{ mmol g}^{-1} \text{ h}^{-1}$ , due to the synergy of the N atoms and the –COOH groups. Very recently, it was found that the significant interaction between the pyridinic N and carbon-based groups (–COOH/C–O–C) helped the desorption of intermediates \*OOH, which subsequently enhanced the  $\text{H}_2\text{O}_2$  selectivity, via the density functional theory (DFT) computation [36]. Therefore, the type and doping mode of dopants play crucial roles in electrochemical  $2e^-$  ORR processes. In addition, the relationship between solvation effect and ORR selectivity has also been reported [37,38]. Therefore, it is necessary to investigate the hydrophilicity and charge of the catalyst.

Metal–organic framework materials (MOFs) have been widely considered as potential templates to produce carbon materials with adjustable heteroatoms, stable carbon skeleton structure, high specific surface area and abundant pore structures [39]. The carbon-based catalysts derived from MOFs are widely studied to be promising in ORR/OER (oxygen reduction reaction), HER (hydrogen evolution reaction) and  $\text{CO}_2\text{RR}$  ( $\text{CO}_2$  reduction reaction) [40–44]. For the electrochemical production of  $\text{H}_2\text{O}_2$ , Sun [45] et al. and Gao [46] et al. demonstrated that MOF-derived Co–N–C single-atom catalysts (SACs) displayed good  $2e^-$  ORR properties in acidic solutions, whereas the same Co–N–C SACs was found to show mainly  $4e^-$  ORR performance in alkaline solutions [47–50]. In some other studies, MOF-derived carbon materials, such as layered porous carbon derived from MOF-5 [51], F-doped porous carbon prepared from MIL-53(Al) [28], NCPs synthesized by ZnPDA (zinc pyridine-2,6-dicarboxylate) [52] and ZIF-8-derived N-doped porous carbon *p*-ZIF [53], are considered for the electrochemical production of  $\text{H}_2\text{O}_2$  in acidic solutions. Concerning the potential applications of  $\text{H}_2\text{O}_2$  in industry, it is also interesting to produce  $\text{H}_2\text{O}_2$  in alkaline solutions. In the present work, ZIF-67 (zeolitic imidazolate-67) was chosen as the precursor to synthesize porous carbon materials with a uniform distributed N dopant. The  $\text{HNO}_3$  (nitric acid) oxidation treatment was carried out to introduce –COOH, and at the same time to remove metal Co from the carbon framework. Finally, the carbon materials co-doped by N and –COOH were used as catalysts to investigate the effects of microstructure, dopant type, contact angle and Zeta potential on the property of  $2e^-$  ORR. The ultra-high formation rate of  $2909.79 \text{ mmol g}^{-1} \text{ h}^{-1}$  for  $\text{H}_2\text{O}_2$  was reached in KOH solution (0.1 M), indicating that this material is a promising  $2e^-$  ORR electrocatalyst.

## 2. Experimental

### 2.1. Reagents and Chemicals

2-Methylimidazole and cobalt nitrate hexahydrate ( $\text{Co}(\text{NO}_3)_2 \cdot 6\text{H}_2\text{O}$ ) were provided from Aladdin Reagent Co., Ltd. (Shanghai, China); 5% Nafion solution was obtained from Aldrich chemical Co., Inc. (Du Pont, Wilmington, DE, USA). Nafion 115 membrane was obtained from Dupont. Carbon cloths (W0S1009) were purchased from Taiwan Carbon Energy Technology Co., Ltd. (Sinero Technology Co., Ltd. Suzhou, China). Methanol ( $\geq 99.5\%$ ), ethanol ( $\geq 99.5\%$ ), nitric acid (65%) and hydrochloric acid (36–38%) were provided from Sinopharm Group Chemical Reagent Co., Ltd. (Shanghai, China). All chemicals were employed without further treatment.

### 2.2. Synthesis of Catalysts

*Synthesis of ZIF-67:* The dissolution of  $\text{Co}(\text{NO}_3)_2 \cdot 6\text{H}_2\text{O}$  (0.5850 g) and 2-methylimidazole (0.9850 g) was carried out in methanol (50 mL) to obtain two solutions. The 2-methylimidazole solution was charged drop-wise into the  $\text{Co}(\text{NO}_3)_2$  solution with vigorous stirring. After stirring for 3 h at ambient temperature, the mixture was kept static for 12 h to obtain the sediment, followed by centrifuging, washing with ethanol and vacuum-drying at  $70^\circ\text{C}$  for 12 h. The collected product was named ZIF-67.

*Synthesis of NPC-900:* A portion of ZIF-67 powder was heated in flowing N<sub>2</sub> at 900 °C for 3 h. The carbonized product was then immersed in 15% concentration HCl solution, followed by stirring slowly for 12 h to eliminate the residual cobalt. After being washed with deionized water to pH = 7, the black powder obtained was vacuum-dried at 70 °C for 12 h. The collected product was named NPC-900.

*Synthesis of O-NPC-T:* In a typical pre-oxidation procedure, NPC-900 (50 mg) was charged into 100 mL of 65% nitric acid. The obtained solution was refluxed at 120 °C for 3 h, followed by washing to pH = 7. The black products were then vacuum-dried at 70 °C for 12 h and named as O-NPC-120. For comparison, the pre-oxidation was also performed at 80 °C and 100 °C, and the obtained products were named O-NPC-80 and O-NPC-100, respectively.

### 2.3. Characterization of Catalysts

The catalyst crystal structure was identified by X-ray diffraction (XRD, Bruker AXS D8: Bruker, Karlsruhe, Germany) under Cu K $\alpha$  radiation. The morphologies and structures were observed by field emission scanning electron microscopy (FESEM, ZEISS-Sigma 500: ZEISS, Munich, Germany) and transmission electron microscopy (TEM, JEOL-JEM-2100, JEOL Ltd., Tokyo, Japan). Fourier-transformed infrared spectroscopy (FT-IR, PE spectroscopy ASCI: Bruker, Karlsruhe, Germany) was employed to study the formation of ZIF-67 precursor and the changes in chemical bonds during pyrolysis. X-ray photoelectron spectroscopy (XPS, KRATOS-AXIS-ULTRA-DLD: KRATOS, Manchester, UK) was used to obtain the surface composition of the catalyst. The C1s, O1s and N1s XPS spectra were analyzed with Casa XPS software version 2.3.23, with 284.6 eV as the charge-corrected reference for C 1s. The degree of carbon defects was characterized by Raman spectroscopy (Raman, HORIBA-Lab RAM-HR: Jobin Yvon, Longjumeau, France). The specific surface area and pore size distribution of the catalysts were measured by the Micromeritics Instrument TriStar II 3020 (Micromeritics Instrument, Norcross, GA, USA) for N<sub>2</sub> adsorption-analytical isotherms, on the basis of the Brunauer–Emmett–Teller (BET) equation and the Barrett–Joyner–Halenda (BJH) method. UV-Vis spectrum was collected on Shimadzu UV-2600 UV-Vis spectrophotometer (Shimadzu, Kyoto, Japan). The Zeta potential of the material surface in aqueous solution was determined using Malvern Zetasizer Nano ZS90 (Malvern Instruments Ltd., Malvern, UK). The content of metallic Co in the material was determined using ICP-MS Agilent 7800 (Agilent, Santa Clara, CA, USA).

### 2.4. Electrochemical Measurements

An electrochemical workstation (CHI 760 B) and Pine Rotator (Instrument model: AFMSRCE, Pine Research Instrumentation, Inc., Durham, NC, USA) were employed to explore the catalytic properties of the electrocatalysts at 25 °C. All the electrochemical characterization was performed in a standardized three-electrode cell. An RRDE (RDE: 0.2475 cm<sup>2</sup>, Pt ring: 0.1866 cm<sup>2</sup>) loaded with catalysts was taken as a working electrode, and a Pt-mesh and saturated Hg/HgO (1 M KOH) electrode were taken as a counter electrode and a reference electrode, respectively.

*Preparation of RRDE working electrode:* The dispersion of the catalyst (5 mg) in an aqueous solution with 1960  $\mu$ L of isopropanol solution ( $V_{\text{isopropanol}}: V_{\text{H}_2\text{O}} = 1 : 3$ ) and Nafion (40  $\mu$ L, 5 wt.%) was conducted under 2 h of sonication, to form the homogeneous catalyst ink. The ink (10  $\mu$ L) was then transferred onto the RRDE surface, followed by drying at ambient temperature in air to synthesize the working electrode. Additionally, the catalyst loading amount was 100  $\mu$ g/cm<sup>2</sup>.

The measurements of cyclic voltammetry (CV) and linear sweep voltammetry (LSV) were carried out from 0 to 1.0 V (vs. *RHE*) in N<sub>2</sub>- or O<sub>2</sub>-saturated 0.1 M KOH electrolytes (pH 13) at a scanning speed of 50 mV s<sup>-1</sup> and 10 mV s<sup>-1</sup>, respectively. The rotation speed of RRDE was 1600 rpm. The ring potential was set at 1.2 V (vs. *RHE*) to quantitatively

detect the  $\text{H}_2\text{O}_2$ . The conversion of all the potentials into reversible hydrogen electrodes (RHE) was performed by the subsequent equation:

$$E_{RHE} = E_{\text{H}_8\text{O}} + 0.0591 \times \text{pH} + 0.098 \text{ (V)} \quad (1)$$

The electron transfer number ( $n$ ), the  $\text{H}_2\text{O}_2$  selectivity ( $\text{H}_2\text{O}_2\%$ ) and the Tafel slope  $\eta$  are computed from the RRDE polarization curve with the subsequent equations:

$$n = \frac{4 \times N \times |I_{\text{disk}}|}{N \times |I_{\text{disk}}| + I_{\text{ring}}} \quad (2)$$

$$\text{H}_2\text{O}_2\% = \frac{200 \times I_{\text{ring}}}{N \times |I_{\text{disk}}| + I_{\text{ring}}} \quad (3)$$

$$\eta = b \log j_k + a \quad (4)$$

where  $I_{\text{disk}}$  is the disk current ( $\text{mA cm}^{-2}$ ),  $I_{\text{ring}}$  is the ring current ( $\text{mA cm}^{-2}$ ).  $N$  is the collection efficiency of Pt ring, which is calculated to be 0.35 (the collection efficiency is obtained with a one-electron reversible  $[\text{Fe}(\text{CN})_6^{4-}]/[\text{Fe}(\text{CN})_6^{3-}]$  system in  $\text{K}_3[\text{Fe}(\text{CN})_6]$  solution).  $j$  indicates the kinetic current density and  $b$  refers to the Tafel slope,  $j_k$  is kinetic current ( $\text{mA cm}^{-2}$ ).

According to the K-L equation, the kinetic current density is calculated as follows:

$$\frac{1}{j} = \frac{1}{j_k} + \frac{1}{j_L} \quad (5)$$

$$j_L = 0.62nFD_{\text{O}_2}^{\frac{2}{3}}v^{-\frac{1}{6}}\omega^{\frac{1}{2}}C_{\text{O}_2} \quad (6)$$

where  $j$  is the measured current density and  $j_k$  and  $j_L$  are the kinetic current and diffusion-limited current densities, respectively.  $n$  is the number of electrons transferred,  $F$  is the Faraday constant ( $96,485 \text{ C mol}^{-1}$ ),  $D_{\text{O}_2}$  is the diffusion coefficient of oxygen ( $1.9 \times 10^{-5} \text{ cm}^2 \text{ s}^{-1}$ ),  $\bar{\nu}$  is the kinematic viscosity of the solution ( $0.01 \text{ cm}^2 \text{ s}^{-1}$ ),  $\omega$  is the angular velocity (in rpm),  $C_{\text{O}_2}$  is the bulk concentration of  $\text{O}_2$  ( $1.2 \times 10^{-3} \text{ mol L}^{-1}$ ).

### 2.5. Determination of $\text{H}_2\text{O}_2$ Production and Faradaic Efficiency

In order to eliminate the occurrence of the reaction of the  $\text{H}_2\text{O}_2$  generated on the counter electrode, the tests were performed in an H-type electrolytic cell equipped with a pretreated Nafion 115 separator. The specific test process was as follows: the catalyst ink was coated on commercial carbon cloth ( $1 \times 1 \text{ cm}^2$ ) and dried at ambient temperature to prepare the working electrode. The cell was filled with KOH solution (40 mL, 0.1 M). Before testing, the cathode compartment was purged with a high-purity oxygen gas for no less than 30 min, and oxygen was kept continuously supplied to the cathode compartment. In situ electrolysis was performed at 0.26 V, 0.36 V and 0.46 V by chronoamperometry for 3 h. A certain amount of electrolyte was taken every 30 min, and the quantification of generated  $\text{H}_2\text{O}_2$  ( $\text{HO}_2^-$ ) was performed by the  $\text{Ce}(\text{SO}_4)_2$  titration approach.



According to the concentration of reduced  $\text{Ce}^{4+}$ , the Faradaic efficiency ( $FE\%$ ) for  $\text{H}_2\text{O}_2$  formation can be obtained with the subsequent formula:

$$FE\% = \frac{Q_{\text{H}_2\text{O}_2}}{Q_{\text{total}}} \times 100\% = \frac{2 C_{\text{H}_2\text{O}_2} V \times F}{Q_{\text{total}}} \times 100\% \quad (8)$$

where  $Q_{\text{H}_2\text{O}_2}$  is the charge consumed to produce  $\text{H}_2\text{O}_2$  (C),  $Q_{\text{total}}$  represents the total charge (C) passed in the chronoamperometric test in 3 h, which was realized by the subtraction of the charges measured in nitrogen-saturated solution from those in oxygen-saturated

one,  $C_{H_2O_2}$  refers to the concentration of  $H_2O_2$  produced ( $\text{mol L}^{-1}$ ),  $V$  is the volume of electrolyte (L),  $i$  denotes the current during electrolysis (A),  $F$  indicates Faraday's constant ( $96,485 \text{ C/mol}$ ) and  $t$  is the electrolysis time (s).

### 3. Results and Discussion

#### 3.1. Synthesis and Characterization of Catalysts

Figure 1a presents the XRD patterns of the prepared material. Clearly all the diffraction peaks are located exactly in the same positions as published in the literature [54,55], proving the successful formation of single-phase ZIF-67. Figure 1b shows the XRD pattern of the pyrolysis product and the oxidation products that were pre-treated by concentrated nitric acid at different temperatures. All these materials show diffraction peaks at  $25.99^\circ$ ,  $42.66^\circ$ ,  $53.62^\circ$  and  $77.66^\circ$ , attributed to the (002), (100), (004) and (110) planes of graphitic carbon, respectively. In the pyrolysis product, the small diffraction peaks at  $44.18^\circ$ ,  $51.56^\circ$  and  $75.78^\circ$  correspond to the (111), (200) and (220) crystal planes of metallic Co (JCPDS: 15-0806). The intensities of these diffraction peaks gradually decrease with the increase in pre-oxidation temperatures. At  $100^\circ\text{C}$  and  $120^\circ\text{C}$ , these diffraction peaks disappear, indicating that the Co element in the material is completely removed after the nitrate acid pre-oxidation treatment. To further study whether there is residual cobalt in the catalyst, the content of metallic Co in the catalyst material is measured by ICP-MS, and the result is shown in Table 1. The Co content decreases with the rising temperature of pre-oxidation. When the pre-oxidation temperature reaches  $100^\circ\text{C}$  and  $120^\circ\text{C}$ , the content of metallic Co is less than the detection limit (0.01%). This result is consistent with the EDS data (0.03%, Figure S2d), indicating almost no metallic Co in the catalyst.

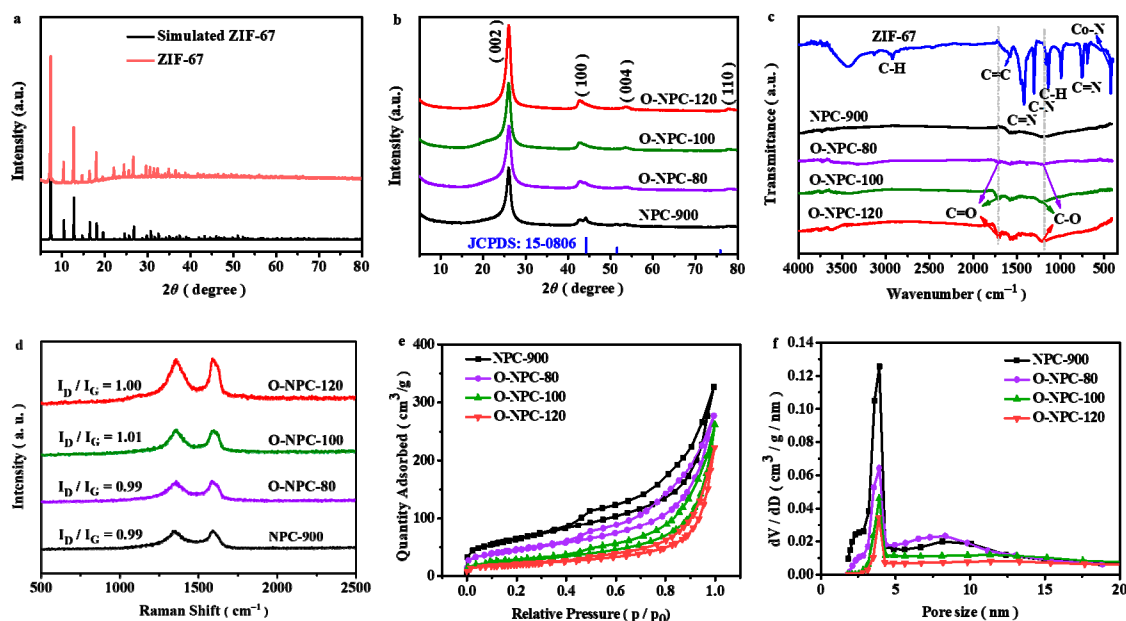


**Figure 1.** XRD patterns of (a) the precursor ZIF-67. (b) NPC-900 and O-NPC-T. (c) FT-IR spectra of ZIF-67, NPC-900 and O-NPC-T. (d) Raman spectra of NPC-900 and O-NPC-T. (e) N<sub>2</sub> adsorption–desorption isotherms of NPC-900 and O-NPC-T at 77K. (f) Pore size distribution of NPC-900 and O-NPC-T.

**Table 1.** Determination of Co content in catalysts by ICP-MS.

Sample	NPC-900	O-NPC-80	O-NPC-100	O-NPC-120
Co (wt %)	0.89	0.16	<0.01	<0.01

Figure 1c shows the FT-IR spectra of corresponding studied materials. For ZIF-67, the typical FT-IR spectrum is obtained [55–58]. The peak at  $3425\text{ cm}^{-1}$  is attributed to the  $-\text{OH}$  stretching vibration;  $1580\text{ cm}^{-1}$  is due to the  $\text{C}=\text{C}$  stretching vibration; the peaks at  $1417\text{ cm}^{-1}$  and  $1303\text{ cm}^{-1}$  can be assigned to the  $\text{C}=\text{N}$  and  $\text{C}-\text{N}$  stretching vibrations. The other two peaks at  $1141\text{ cm}^{-1}$  and  $755\text{ cm}^{-1}$  belong to the  $\text{C}-\text{H}$  and  $\text{C}=\text{N}$  bending vibrations. In summary, all the peaks are derived from the vibrations of the imidazole ring. In addition, the peak at  $425\text{ cm}^{-1}$  refers to the vibration of  $\text{Co}-\text{N}$  coordination bonds. Therefore, combined with the XRD characterizations, it shows clearly that ZIF-67 is successfully synthesized. After the pyrolysis treatment at  $900\text{ }^\circ\text{C}$ , the vibration peaks of  $-\text{OH}$  and the imidazole ring disappear, indicating the decomposition of the ZIF-67 precursor to form carbon-related products. After the pre-oxidation treatment, two newly developed peaks at  $\sim 1700\text{ cm}^{-1}$  and  $\sim 1205\text{ cm}^{-1}$  are attributable to the stretching vibration of  $\text{C}=\text{O}$  and  $\text{C}-\text{O}$ , showing the successful integration of  $\text{O}$ -containing functional groups into the pyrolysis products.

Carbon defect is a significant indicator to determine the catalytic ability of carbons for  $\text{H}_2\text{O}_2$  formation via the  $2e^-$  ORR pathway [51,59]. To characterize the possible carbon defects in our material, Raman spectrum is collected (Figure 1d). The D-band and G-band appear at  $\sim 1350\text{ cm}^{-1}$  and  $\sim 1600\text{ cm}^{-1}$  in the four studied materials. Typically, the intensity ratio of D-band to G-band ( $I_D/I_G$ ) describes the relative defect contents in carbon materials, mainly due to the fact that D-band and G-band are associated with the disordered and ordered crystalline  $\text{sp}^2\text{-C}$ , respectively [23]. It is generally believed that the larger the ratio, the higher the amounts of defects. However, it is found from Figure 1d that the  $I_D/I_G$  are 0.99, 0.99, 1.01 and 1.00 for NPC-900, O-NPC-80, O-NPC-100 and O-NPC-120, respectively. This result indicates that the relative carbon defect contents are quite similar in the four studied carbon materials. The specific surface area and porosity of the material are further calculated by  $\text{N}_2$ -sorption isotherms. At the relative pressure of  $0.4 < p/p_0 < 1.0$ , the hysteresis loops are found in all samples, indicating the generation of mesoporous structures (Figure 1e). The curves of pore diameter distribution verify the existence of a mesoporous structure with apparent peaks of around  $2.3\sim 4.3\text{ nm}$  (Figure 1f). Meanwhile, stacking pores with pore size around  $5.5\sim 10\text{ nm}$  are also observed in NPC-900 and O-NPC-80. The calculated pore volumes of NPC-900 ( $0.4913\text{ cm}^3/\text{g}$ ) and O-NPC-80 ( $0.4196\text{ cm}^3/\text{g}$ ) are significantly larger than those of O-NPC-100 ( $0.3822\text{ cm}^3/\text{g}$ ) and O-NPC-120 ( $0.3223\text{ cm}^3/\text{g}$ ). Furthermore, the Brunauer–Emmett–Teller (BET) surface areas of NPC-900, O-NPC-80, O-NPC-100 and O-NPC-120 are  $226.40\text{ m}^2/\text{g}$ ,  $157.65\text{ m}^2/\text{g}$ ,  $92.11\text{ m}^2/\text{g}$  and  $56.58\text{ m}^2/\text{g}$ , respectively. The pre-oxidation temperature increases with the gradually decreasing specific surface area of the material, probably due to the collapse of the pore structure. This conclusion can also be drawn from the observation of the microstructure evolution of the catalysts (Figures S1 and S2).

### 3.2. $2e^-$ ORR Performance of Catalysts

The half-wave potential ( $E_{1/2}$ ) is a key index to assess the ORR electrocatalyst activity [60]. Based on the linear sweep voltammetry plots, the  $E_{1/2}$  of NPC-900 is  $0.78\text{ V}$ , while it is  $0.74\text{ V}$ ,  $0.75\text{ V}$  and  $0.73\text{ V}$  for O-NPC-80, O-NPC-100 and O-NPC-120, respectively (Figure 2a). The  $E_{1/2}$  of O-NPC-120 is very similar to the thermodynamic potential of  $2e^-$  ORR ( $\approx 0.7\text{ V}$ ) [56,58], indicating that it has the best  $2e^-$  ORR activity. Meanwhile, the ring current of O-NPC-120 reaches  $1.80\text{ mA cm}^{-2}$ , which is the highest one among the four studied materials. The CV curves of the catalysts indicate obvious ORR catalytic activity of these carbon materials (Figure S4). Figure 2b,c show the electron transfer number and selectivity of  $\text{H}_2\text{O}_2$  that were obtained according to the plots of Figure 2a. Clearly, O-NPC-120 shows the best performance, with  $n = 2.33$ , and the selectivity reaches  $83.10\%$ . The electron transfer number was further calculated through the K-L equation (Figure S5), and the result was found to be consistent with the RRDE measurement. To gain a further understanding of the  $2e^-$  ORR performance, the Tafel slope values are calculated and the results are presented in Figure 2d. It is found that the values are between  $35$  and  $47\text{ mV dec}^{-1}$  for

the four studied materials. This value is smaller than some carbon catalysts reported in the literature [23,61–66], indicating that ZIF-67-derived carbon has much faster kinetics for the  $2e^-$  ORR reaction. The effects of catalyst loading are studied and the results are presented in Figure S6. Clearly, when the catalyst loading is  $100 \text{ } \mu\text{g}/\text{cm}^2$ , the electrode shows the best  $2e^-$  ORR performance. Figure 2e shows the stability test for 10 h. Both the ring current and the disk current have no obvious attenuation after 10 h consecutive recording, indicating the quite super stability of the catalyst. The ORR performance of the glassy carbon electrode (GCE) without the loading of catalysts was evaluated and the results are comparably shown in Figure S3. This result indicates that the major contribution of  $\text{H}_2\text{O}_2$  production comes from the catalytic activity of O-NPC-120.

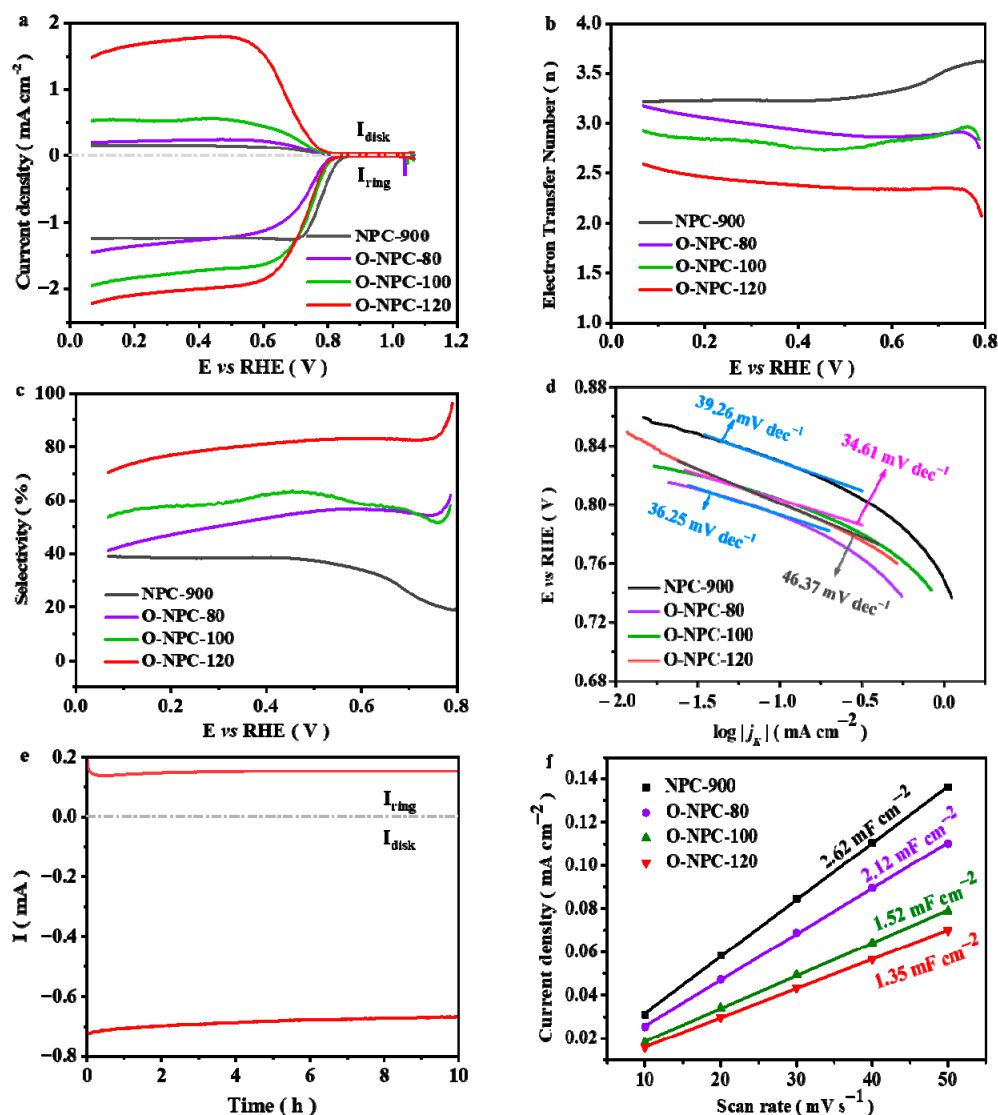


**Figure 2.** The catalyst ORR property in KOH electrolyte (0.1 M): (a) The catalyst RRDE polarization curves at 1600 rpm and a scan rate of  $10 \text{ mV s}^{-1}$ . Current density was normalized to loading and BET. (b) Electron transfer number and (c)  $\text{H}_2\text{O}_2$  selectivity of catalysts. (d) Tafel slope of catalysts. (e) Stability test of O-NPC-120 at a fixed disk potential of 0.36 V. (f) The capacitance current densities (obtained from Figure S4) tested at 0.963 V (vs. RHE) as a function of scanning rate. The slope value refers to the double-layer capacitance ( $C_{dl}$ ).

To further understand the important parameters determining the  $2e^-$  ORR activity and selectivity, the electrochemical double-layer capacitance ( $C_{dl}$ ) of the four carbon materials is tested. According to Figure 2g, the  $C_{dl}$  of NPC-900, O-NPC-80, O-NPC-100 and O-NPC-120

is  $2.62 \text{ mF cm}^{-2}$ ,  $2.12 \text{ mF cm}^{-2}$ ,  $1.52 \text{ mF cm}^{-2}$  and  $1.35 \text{ mF cm}^{-2}$ , respectively. Considering that the electrochemical active surface area (ECSA) is positively proportional to  $C_{dl}$  [67,68], this result shows that O-NPC-120 has the smallest ECSA among the four materials. In addition, the Raman analysis has proved that there is no significant difference of carbon defect contents in the four studied carbon materials (Figure 1d).

### 3.3. Production Test of $\text{H}_2\text{O}_2$

In order to obtain the working potential for the formation of  $\text{H}_2\text{O}_2$ , and to eliminate the reduction of the generated  $\text{H}_2\text{O}_2$  during the oxygen reduction process, the reduction reaction test of  $\text{H}_2\text{O}_2$  was carried out (Figure S8). The currents that appear over 0.79 V and below 0.25 V are assigned to the currents of oxidation and reduction of  $\text{H}_2\text{O}_2$  [29], respectively. Therefore, the applied voltages of 0.26 V, 0.36 V and 0.46 V were selected in the  $\text{H}_2\text{O}_2$  production rate measurement experiments. The amount of  $\text{H}_2\text{O}_2$  produced is calculated by the spectroscopic results (Figure S9), which are normalized by electrolysis time and catalyst loading to obtain the  $\text{H}_2\text{O}_2$  production rate (Figure 3a). It is observed that the  $\text{H}_2\text{O}_2$  amount increases gradually with the electrolysis time. The O-NPC-120 electrocatalyst exhibits a high  $\text{H}_2\text{O}_2$  production rate of  $2907.79 \text{ mmol g}_{\text{catalyst}}^{-1} \text{ h}^{-1}$  at 0.36 V, significantly larger than the  $\text{H}_2\text{O}_2$  production rate reported [69–75] (Table S5). Figure 3b is the faradaic efficiency diagram of O-NPC-120. The Faradaic efficiency reaches 95.63% at 0.36 V, much better than that at 0.26 V and 0.46 V.

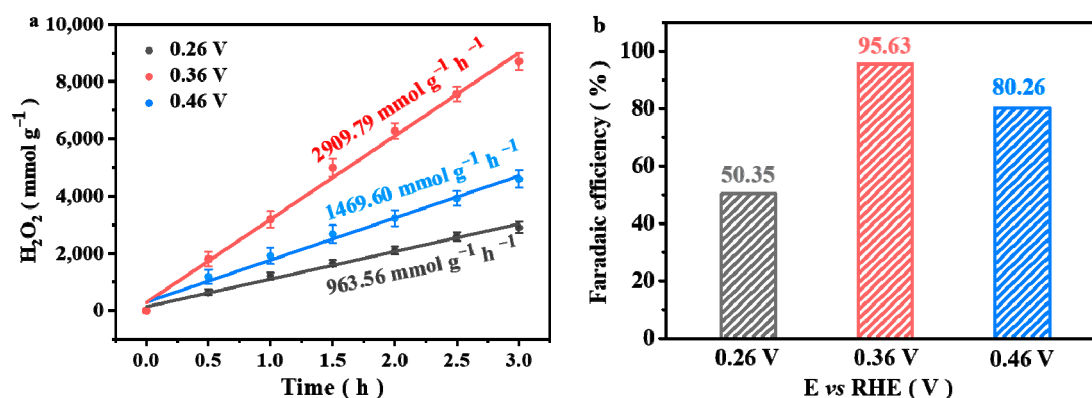


Figure 3. (a)  $\text{H}_2\text{O}_2$  production rate; (b) the corresponding faradaic efficiency (FE%).

### 3.4. Catalytic Mechanism Analysis

Hydrophilicity is a critical feature for  $\text{H}_2\text{O}_2$  generation [66]. To examine the wetting ability of the catalysts to the 0.1 M KOH electrolyte solution, contact angle tests were performed (Figure 4). The contact angles of NPC-900, O-NPC-80, O-NPC-100 and O-NPC-120 are  $143.5^\circ$ ,  $73.5^\circ$ ,  $41.3^\circ$  and  $24.0^\circ$ . This result shows that the contact angle decreases dramatically with the pre-oxidation treatment temperatures. This is attributed to the integration of O-containing functional groups, which increases the hydrophilicity of the carbon material. The good hydrophilicity may facilitate the mutual interaction between the carbon catalyst and the electrolyte, and contribute to the diffusion of  $\text{O}_2$ .

Zeta potential is another important factor affecting ORR [76]. The Zeta potentials of NPC-900, O-NPC-80, O-NPC-100 and O-NPC-120 are measured to be  $-6.04 \text{ mV}$ ,  $-29.6 \text{ mV}$ ,  $-39.4 \text{ mV}$  and  $-40.4 \text{ mV}$ , respectively (Figure 5a). It can be seen that Zeta potential becomes more negative with the increase in pre-oxidation treatment temperatures, with O-NPC-120 showing the most negative Zeta value. This result indicates that O-NPC-120 has the strongest desorption ability for the adsorbed intermediate species  $\text{OOH}^-$ , due to the coulombic repulsion effects of this carbon material to negatively charged species. It is well established in the literature that the easy desorption of  $\text{OOH}^-$  from the catalyst surface is beneficial for the  $2e^-$  ORR reaction, therefore O-NPC-120 shows the best catalytic performance for  $\text{H}_2\text{O}_2$  production.



Figure 4. Contact angle pictures of catalysts: (a) NPC-900. (b) O-NPC-80. (c) O-NPC-100. (d) O-NPC-120.

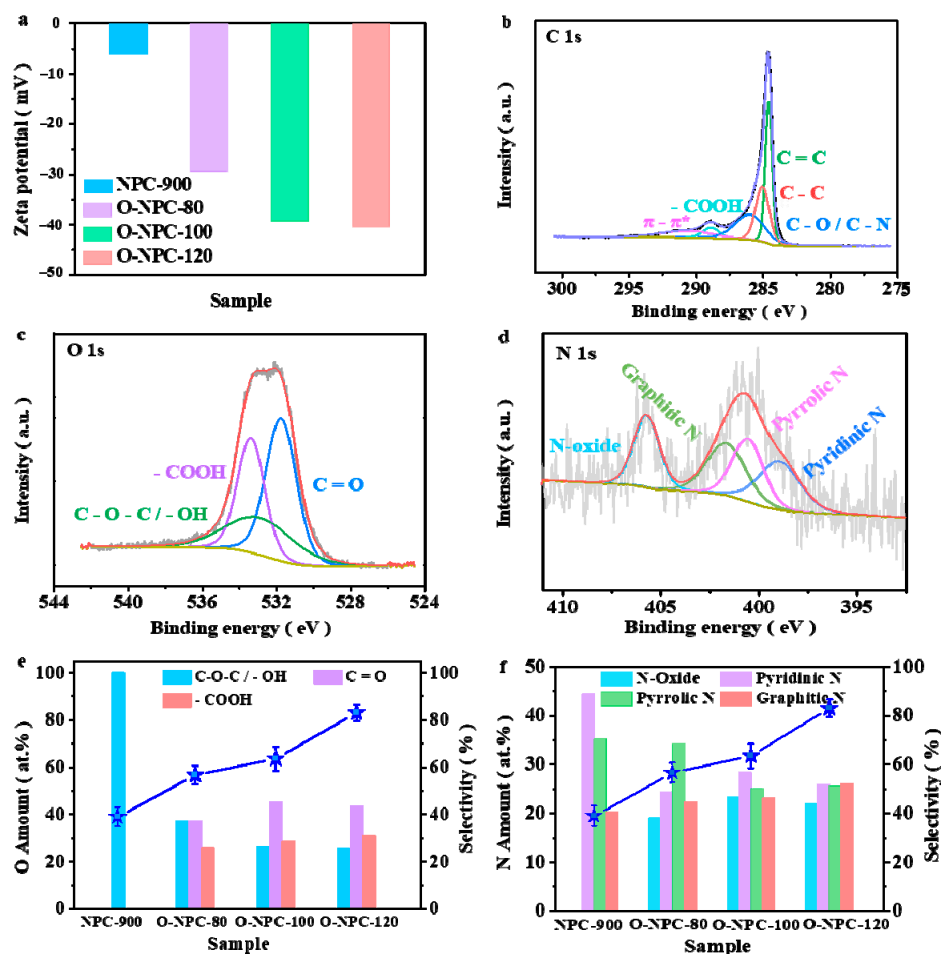


Figure 5. (a) Zeta potential of catalysts in water (pH = 7). XPS spectra of O-NPC-120 (b) C1s, (c) O1s, (d) N1s. (e) A plot of the relationship between the atomic ratio of O and  $\text{H}_2\text{O}_2$  selectivity. (f) A plot of the relationship between the atomic ratio of N and  $\text{H}_2\text{O}_2$  selectivity.

The chemical components and bonding states are characterized by XPS, so as to determine the active centres of the catalyst (Figures 5b–d and S11–S13). Clearly, the strong signals of C1s, N1s and O1s are found at  $\sim 285.0$  eV,  $\sim 401.0$  eV and  $\sim 531.6$  eV, respectively (the specific contents of C, N and O are shown in Table S1). The C1s signal of O-NPC-120 can be decomposed into five types (Figure 5b), namely,  $\text{sp}^2$ -C: C=C (284.60 eV),  $\text{sp}^3$ -C: C-C (285.06 eV), C-O/C-N (286.00 eV), -COOH (288.89 eV) and  $\pi \rightarrow \pi^*$  (290.61 eV). The corresponding atomic percentages are 32.01%, 25.29%, 25.1%, 5.95% and 11.65% (Table S2). The O1s signal is decomposed into three types (Figure 5c), namely, C=O (531.76 eV), C-O-C/-OH (532.40 eV) and -COOH (533.38 eV), and their relative concentrations are 43.50%, 25.43% and 31.07% (Table S3). In summary, the successful integration of -COOH into the carbon framework is realized after the nitric acid pre-oxidation treatment. It is also

observed that the content of –COOH increases with the increase in pre-oxidation temperatures (Table S3). The N1s signal at ~400 eV can be decomposed into three types (Figure 5d), namely, pyridinic N (398.54 eV), pyrrolic N (400.56 eV) and graphitic N (401.63 eV). Another peak at 405.80 eV is due to the formation of N–oxide. The corresponding atomic percentages of various N species are shown in Table S4. In order to understand the contributions of different N- and O-containing species to the catalytic activity, the variations of H<sub>2</sub>O<sub>2</sub> selectivity versus atomic percentages of O and N species are plotted in Figure 5e,f, respectively. Clearly, the selectivity of H<sub>2</sub>O<sub>2</sub> increases with the increase in –COOH and graphitic N contents. Therefore, we propose that both the –COOH and graphitic N are the catalytic centres for the 2e<sup>−</sup> ORR reaction. Furthermore, DFT simulation results have confirmed the improvement effects of the coupled N/COOH complexes on the improved adsorption of O<sub>2</sub> [35,77,78]. Moreover, the nitrogen-based and COOH-based groups may also play the roles of the intramolecular acid/base to aid the catalytic reactions [79,80]. Therefore, we believe that the excellent performance of O-NPC-120 is due to the joint contributions of graphite N and –COOH.

At last, the active site density is calculated according to the following formula [68]:

$$\begin{aligned} \text{ASSD} &= \frac{m_{\text{catalyst}} \times \text{O}\%(\text{at}\%) \times (-\text{COOH}\%)(\text{at}\%) }{m_{\text{catalyst}} \times \text{BET}(\text{m}^2 \text{g}^{-1})} + \frac{m_{\text{catalyst}} \times \text{N}\%(\text{at}\%) \times (\text{Graphitic N}\%)(\text{at}\%) }{m_{\text{catalyst}} \times \text{BET}(\text{m}^2 \text{g}^{-1})} \\ &= \left[ \frac{\text{O}\%(\text{at}\%) \times (-\text{COOH}\%)(\text{at}\%) }{\text{BET}} + \frac{\text{N}\%(\text{at}\%) \times (\text{Graphitic N}\%)(\text{at}\%) }{\text{BET}} \right] \times 1000 \text{ (mg m}^{-2}\text{)} \end{aligned} \quad (9)$$

$m_{\text{catalyst}}$  is the mass of catalyst (g); O%(at%) and N%(at%) are the content of O1s and N1s characterized by XPS; –COOH%(at%) and graphitic N%(at%) are the content of –COOH and graphitic N obtained by XPS deconvolution of O1s and N1s.

It can be seen from Table 2 that with the increasing pre-oxidation treatment temperature, the active site density gradually increases, which also makes the activity and selectivity of 2e<sup>−</sup> ORR increase sequentially.

**Table 2.** Calculation results of active site density.

Sample	NPC-900	O-NPC-80	O-NPC-100	O-NPC-120
ASSD	0.0112	0.2036	0.4202	0.8449

#### 4. Conclusions

ZIF-67 was used as the precursor, and the oxygen-containing functional group (–COOH) was successfully introduced into the carbon skeleton through high-temperature carbonization and a concentrated nitric acid oxidation reaction. The results show that the electron transfer number of O-NPC-120 is 2.33, and the selectivity of H<sub>2</sub>O<sub>2</sub> is 83.10%. The high H<sub>2</sub>O<sub>2</sub> formation rate of –2909.79 mmol g<sub>catalyst</sub><sup>−1</sup> h<sup>−1</sup> was obtained with O-NPC-120 at 0.36 V. The superior property of this catalyst is mostly due to the following aspects: (1) The graphitic N and –COOH functional groups act as catalytic sites, and they work together to greatly enhance the performance of 2e<sup>−</sup> ORR. (2) The catalyst has good hydrophilicity, which can promote the mutual contact between the catalyst and electrolyte and contribute to the diffusion of O<sub>2</sub>. (3) The catalyst has the largest negative Zeta potential value, which is of benefit to the desorption of adsorbed intermediate OOH<sup>−</sup>. The present work is expected to be helpful to rationally design efficient carbon-based catalysts for the production of H<sub>2</sub>O<sub>2</sub>.

**Supplementary Materials:** The following supporting information can be downloaded at: <https://www.mdpi.com/article/10.3390/nano13071188/s1>, Figure S1: SEM image of the catalyst. (a) ZIF-67. (b) NPC-900. (c) O-NPC-80. (d) O-NPC-100. (e) O-NPC-120; Figure S2: TEM images of (a) ZIF-67 and (b) NPC-900. (c) HRTEM image of O-NPC-120. (d) STEM-mapping images and the EDS data of O-NPC-120. (e–h) EDS of O-NPC-120; Figure S3: Comparison of 2e<sup>−</sup> ORR performance between empty glassy carbon electrode (GCE) and catalyst loading GCE. (a) RRDE polarization curve. (b) electron transfer number. (c) H<sub>2</sub>O<sub>2</sub> selectivity; Figure S4: CV curves of the catalysts at 1600 rpm

and  $50 \text{ mV s}^{-1}$  in  $\text{N}_2$  and  $\text{O}_2$  saturated electrolyte. (a) NPC-900. (b) O-NPC-80. (c) O-NPC-100. (d) O-NPC-120. All dashed lines:  $\text{N}_2$ ; all solid lines:  $\text{O}_2$ ; Figure S5: LSV curves of (a) NPC-900, (c) O-NPC-80, (e) O-NPC-100, (g) O-NPC-120 measured at different rotation speeds in  $\text{O}_2$  saturated 0.1 M KOH. (b) NPC-900, (d) O-NPC-80, (f) O-NPC-100, (h) O-NPC-120 are Koutecky–Levich plots based on corresponding LSV curves; Figure S6: Effect of O-NPC-120 loading on catalytic performance of  $2\text{e}^-$  ORR. (a) RRDE polarization curve. (b) electron transfer number. (c)  $\text{H}_2\text{O}_2$  selectivity; Figure S7: Cyclic voltammogram in the non-faradic potential region at varying scan rates for the samples of (a) NPC-900. (b) O-NPC-80. (c) O-NPC-100. (d) O-NPC-120; Figure S8: LSV curves of O-NPC-120 in 0.1M KOH solution with  $\text{H}_2\text{O}_2$  concentrations of 0 mM, 1 mM, 2 mM, and 3 mM; Figure S9: (a) UV-Vis spectra of  $\text{Ce}^{4+}$  solutions with different concentrations. (b) is the standard curve corresponding to (a). Figure S10: i-t curves of O-NPC-120 in 0.1 M KOH electrolyte under different voltages. (a) 0.26 V. (b) 0.36 V. (c) 0.46 V. Loading capacity of catalyst:  $100 \mu\text{g}/\text{cm}^2$ ; Figure S11: The XPS-characterized C1s spectra of (a) NPC-900, (b) O-NPC-80 and (c) O-NPC-100, respectively; Figure S12: O1s spectra characterized by XPS (a) NPC-900, (b) O-NPC-80 and (c) O-NPC-100, respectively; Figure S13: N1s spectra characterized by XPS (a) NPC-900, (b) O-NPC-80 and (c) O-NPC-100, respectively; Table S1: C, N, O contents of catalysts detected by XPS; Table S2: Different C types and contents in catalysts determined from XPS analysis results; Table S3: Different O types and contents in catalysts determined from XPS analysis results; Table S4: Different N types and contents in catalysts determined from XPS analysis results; Table S5:  $2\text{e}^-$  ORR performance of some carbon-based catalysts [19,23,31,59,62–76,81].

**Author Contributions:** Conceptualization, L.S. (Liping Sun), L.H. and H.Z.; Methodology, L.S. (Lina Sun); Software, L.H.; Formal analysis, L.S. (Lina Sun); Investigation, L.S. (Liping Sun); Resources, L.H.; Data curation, L.S. (Lina Sun); Writing—original draft, L.S. (Lina Sun); Writing—review & editing, L.S. (Liping Sun) and H.Z.; Supervision, Hui Zhao; Project administration, L.H. and H.Z.; Funding acquisition, L.S. (Liping Sun). All authors have read and agreed to the published version of the manuscript.

**Funding:** National Natural Science Foundation of China: 51872078. National Natural Science Foundation of China: 52272197.

**Data Availability Statement:** The data presented in this study are available on request from the corresponding author.

**Acknowledgments:** The project was supported by National Natural Science Foundation of China (51872078, 52272197), Heilongjiang Provincial Natural Science Foundation of China (LH2020E105).

**Conflicts of Interest:** The authors declare no conflict of interest.

## References

1. Myers, R.L. *The 100 Most Important Chemical Compounds: A Reference Guide*; Greenwood Press: Westport, CT, USA, 2007.
2. Kato, S.; Jung, J.U.; Suenobu, T.; Fukuzumi, S. Production of hydrogen peroxide as a sustainable solar fuel from water and dioxygen. *Energy Environ. Sci.* **2013**, *6*, 3756–3764. [[CrossRef](#)]
3. Bao, Z.K.; Zhao, J.Y.; Zhang, S.J.; Ding, L.; Peng, X.G.; Wang, G.L.; Zhao, Z.J.; Zhong, X.; Yao, Z.H.; Wang, J.G. Synergistic effect of doped nitrogen and oxygen—Containing functional groups on electrochemical synthesis of hydrogen peroxide. *J. Mater. Chem. A* **2022**, *10*, 4749–4757. [[CrossRef](#)]
4. Hage, R.; Lienke, A. Applications of Transition-Metal Catalysts to Textile and Wood-Pulp Bleaching. *Angew. Chem. Int. Ed.* **2006**, *45*, 206–222. [[CrossRef](#)]
5. Ding, J.; Huang, J.; Zhang, Q.; Wei, Z.M.; He, Q.Y.; Chen, Z.Y.; Liu, Y.H.; Su, X.Z.; Zhai, Y.M. A hierarchical monolithic cobalt–single–atom electrode for efficient hydrogen peroxide production in acid. *Catal. Sci. Technol.* **2022**, *12*, 2416–2419. [[CrossRef](#)]
6. Mahmood, A.; Eqan, M.; Pervez, S.; Alghamdi, H.A.; Tabinda, A.B.; Yasar, A.; Brindhadevi, K.; Pugazhendhi, A. COVID-19 and frequent use of hand sanitizers; human health and environmental hazards by exposure pathways. *Sci. Total Environ.* **2020**, *742*, 140561. [[PubMed](#)]
7. Pfeleiderer, G.; Riedl, H.J. Production of Hydrogen Peroxide. U.S. Patent 2158525, 16 May 1939.
8. Yi, Y.H.; Wang, L.; Li, G.; Guo, H.C. A review on research progress in the direct synthesis of hydrogen peroxide from hydrogen and oxygen: Noble–metal catalytic method, fuel–cell method and plasma method. *Catal. Sci. Technol.* **2016**, *6*, 1593–1610.
9. Yang, S.; Verdaguer-Casadevall, A.; Arnarson, L.; Silvioli, L.; Čolić, V.; Frydendal, R.; Rossmeisl, J.; Chorkendorff, I.; Stephens, I.E. Toward the Decentralized Electrochemical Production of  $\text{H}_2\text{O}_2$ : A Focus on the Catalysis. *ACS Catal.* **2018**, *8*, 4064–4081. [[CrossRef](#)]

10. Berl, E. A New Cathodic Process for the Production of H<sub>2</sub>O<sub>2</sub>. *Trans. Electrochem. Soc.* **1939**, *76*, 359–369.
11. Otsuka, K.; Yamanaka, I. One step synthesis of hydrogen peroxide through fuel cell reaction. *Electrochim. Acta* **1990**, *2*, 319–322. [[CrossRef](#)]
12. Siahrostami, S.; Verdaguer-Casadevall, A.; Karamad, M.; Deiana, D.; Malacrida, P.; Wickman, B.; Escudero-Escribano, M.; Paoli, E.A.; Frydendal, R.; Hansen, T.W.; et al. Enabling direct H<sub>2</sub>O<sub>2</sub> production through rational electrocatalyst design. *Nat. Mater.* **2013**, *12*, 1137–1143. [[CrossRef](#)]
13. Liu, G.; Niu, P.; Sun, C.H.; Smith, S.C.; Chen, Z.G.; Lu, G.Q.; Cheng, H.M. Unique Electronic Structure Induced High Photoreactivity of Sulfur-Doped Graphitic C<sub>3</sub>N<sub>4</sub>. *J. Am. Chem. Soc.* **2010**, *132*, 11642–11648. [[CrossRef](#)] [[PubMed](#)]
14. Zhu, Z.D.; Pan, H.H.; Murugananthan, M.; Gong, J.Y.; Zhang, Y.R. Visible light-driven photocatalytically active g-C<sub>3</sub>N<sub>4</sub> material for enhanced generation of H<sub>2</sub>O<sub>2</sub>. *Appl. Catal. B* **2018**, *232*, 19–25. [[CrossRef](#)]
15. Jirkovsky, J.S.; Panas, I.; Ahlberg, E.; Halasa, M.; Romani, S.; Schiffrin, D.J. Single atom hot-spots at Au–Pd nanoalloys for electrocatalytic H<sub>2</sub>O<sub>2</sub> production. *J. Am. Chem. Soc.* **2011**, *133*, 19432–19441. [[CrossRef](#)] [[PubMed](#)]
16. Verdaguer-Casadevall, A.; Deiana, D.; Karamad, M.; Siahrostami, S.; Malacrida, P.; Hansen, T.W.; Rossmeisl, J.; Chorkendorff, I.; Stephens, I.E. Trends in the electrochemical synthesis of H<sub>2</sub>O<sub>2</sub>: Enhancing activity and selectivity by electro-catalytic site engineering. *Nano Lett.* **2014**, *14*, 1603–1608. [[CrossRef](#)]
17. Fellingner, T.P.; Frédéric, H.; Strasser, P.; Antonietti, M. Mesoporous Nitrogen-Doped Carbon for the Electrocatalytic Synthesis of Hydrogen Peroxide. *J. Am. Chem. Soc.* **2012**, *134*, 4072–4075. [[CrossRef](#)]
18. Park, J.; Nabae, Y.; Hayakawa, T.; Kakimoto, M. Highly Selective Two-Electron Oxygen Reduction Catalyzed by Mesoporous Nitrogen-Doped Carbon. *ACS Catal.* **2014**, *4*, 3749–3754. [[CrossRef](#)]
19. Sheng, X.; Daems, N.; Geboes, B.; Kurttepli, M.; Bals, S.; Breugelmans, T.; Hubin, A.; Vankelecoma, I.F.J.; Pescarmona, P.P. N-doped ordered mesoporous carbons prepared by a two-step nanocasting strategy as highly active and selective electrocatalysts for the reduction of O<sub>2</sub> to H<sub>2</sub>O<sub>2</sub>. *Appl. Catal. B* **2015**, *176–177*, 212–224. [[CrossRef](#)]
20. Roldán, L.; Truong-Phuoc, L.; Ansón-Casaos, A.; Pham-Huu, C.; García-Bordejé, E. Mesoporous carbon doped with N, S heteroatoms prepared by one-pot auto-assembly of molecular precursor for electrocatalytic hydrogen peroxide synthesis. *Catal. Today* **2018**, *301*, 2–10. [[CrossRef](#)]
21. Cheng, X.Y.; Dou, S.S.; Qin, G.H.; Wang, B.Z.; Yan, P.X.; Isimjan, T.T.; Yang, X.L. Rational design of highly selective nitrogen-doped Fe<sub>2</sub>O<sub>3</sub>-CNTs catalyst towards H<sub>2</sub>O<sub>2</sub> generation in alkaline media. *Int. J. Hydrogen Energy* **2020**, *45*, 6128–6137. [[CrossRef](#)]
22. Palm, I.; Kibena-Pöldsepp, E.; Lilloja, J.; Käärik, M.; Kikas, A.; Kisand, V.; Merisalu, M.; Treshchalov, A.; Paiste, P.; Leis, J.; et al. Impact of ball-milling of carbide-derived carbons on the generation of hydrogen peroxide via electroreduction of oxygen in alkaline media. *Electroanal. Chem.* **2020**, *878*, 114690. [[CrossRef](#)]
23. Sa, Y.J.; Kim, J.H.; Joo, S.H. Active edge-site-rich carbon nanocatalysts with enhanced electron transfer for efficient electrochemical hydrogen peroxide production. *Angew. Chem. Int. Ed.* **2019**, *58*, 1100–1105. [[CrossRef](#)] [[PubMed](#)]
24. Yi, L.H.; Hu, Y.; Fei, J.J.; Li, J.; Yang, C.G.; Wang, X.Y. Carbon-supported Pd–Co nanocatalyst as highly active anodic electrocatalyst for direct borohydride/hydrogen peroxide fuel cells. *J. Solid State Electrochem.* **2019**, *23*, 1739–1748. [[CrossRef](#)]
25. Liu, C.W.; Wei, Y.C.; Wang, K.W. Preparation and characterization of carbon-supported Pt–Au cathode catalysts for oxygen reduction reaction. *J. Coll. Interf. Sci.* **2009**, *336*, 654–657. [[CrossRef](#)] [[PubMed](#)]
26. Qu, L.; Liu, Y.; Baek, J.B.; Dai, L. Nitrogen-doped graphene as efficient metal-free electrocatalyst for oxygen reduction in fuel cells. *ACS Nano* **2010**, *4*, 1321–1326. [[CrossRef](#)]
27. Guo, D.; Shibuya, R.; Akiba, C.; Saji, S.; Kondo, T.; Nakamura, J. Active sites of nitrogen-doped carbon materials for oxygen reduction reaction clarified using model catalysts. *Science* **2016**, *351*, 361–365. [[CrossRef](#)]
28. Zhao, K.; Su, Y.; Quan, X.; Liu, Y.; Chen, S.; Yu, H. Enhanced H<sub>2</sub>O<sub>2</sub> production by selective electrochemical reduction of O<sub>2</sub> on fluorine-doped hierarchically porous carbon. *J. Catal.* **2018**, *357*, 118–126. [[CrossRef](#)]
29. Sun, Y.Y.; Sinev, I.; Ju, W.; Bergmann, A.; Dresch, S.; Kühl, S.; Spöri, C.; Schmies, H.; Wang, H.; Bernsmeier, D.; et al. Strasser, Efficient Electrochemical Hydrogen Peroxide Production from Molecular Oxygen on Nitrogen-Doped Mesoporous Carbon Catalysts. *ACS Catal.* **2018**, *8*, 2844–2856. [[CrossRef](#)]
30. Iglesias, D.; Giuliani, A.; Melchionna, M.; Marchesan, S.; Criado, A.; Nasi, L.; Bevilacqua, M.; Tavagnacco, C.; Vizza, F.; Prato, M.; et al. N-Doped Graphitized Carbon Nanohorns as a Forefront Electrocatalyst in Highly Selective O<sub>2</sub> Reduction to H<sub>2</sub>O<sub>2</sub>. *Chem* **2018**, *4*, 106–123. [[CrossRef](#)]
31. Han, L.; Sun, Y.Y.; Li, S.; Cheng, C.; Halbig, C.E.; Feicht, P.; Hübner, J.L.; Strasser, P.; Eigler, S. In-Plane Carbon Lattice-Defect Regulating Electrochemical Oxygen Reduction to Hydrogen Peroxide Production over Nitrogen-Doped Graphene. *ACS Catal.* **2019**, *9*, 1283–1288. [[CrossRef](#)]
32. Babaei-Sati, R.; Parsa, J.B. Electrogeneration of H<sub>2</sub>O<sub>2</sub> using graphite cathode modified with electrochemically synthesized polypyrrole/MWCNT nanocomposite for electro-Fenton process. *J. Ind. Eng. Chem.* **2017**, *52*, 270–276. [[CrossRef](#)]
33. Huynh, T.T.; Tsai, M.C.; Pan, C.J.; Su, W.N.; Chan, T.S.; Lee, J.F.; Hwang, B.-J. Synergetic Electrocatalytic Activities Towards Hydrogen Peroxide: Understanding the Ordered Structure of PdNi Bimetallic Nanocatalysts. *Electrochem. Commun.* **2019**, *101*, 93–98. [[CrossRef](#)]
34. Xia, C.; Xia, Y.; Zhu, P.; Fan, L.; Wang, H.T. Direct electrosynthesis of pure aqueous H<sub>2</sub>O<sub>2</sub> solutions up to 20% by weight using a solid electrolyte. *Science* **2019**, *366*, 226–231. [[CrossRef](#)] [[PubMed](#)]

35. Zhao, H.Y.; Shen, X.Q.; Chen, Y.; Zhang, S.-N.; Gao, P.; Zhen, X.J.; Li, X.-H.; Zhao, G.H. A COOH-terminated nitrogen-doped carbon aerogel as a bulk electrode for completely selective two-electron oxygen reduction to H<sub>2</sub>O<sub>2</sub>. *Chem. Commun.* **2019**, *55*, 6173–6176. [[CrossRef](#)] [[PubMed](#)]
36. Qin, M.C.; Fan, S.Y.; Wang, L.; Gan, G.Q.; Wang, X.Y.; Cheng, J.; Hao, Z.P.; Li, X.Y. Oxygen and nitrogen co-doped ordered mesoporous carbon materials enhanced the electrochemical selectivity of O<sub>2</sub> reduction to H<sub>2</sub>O<sub>2</sub>. *J. Colloid Interface Sci.* **2020**, *562*, 540–549. [[CrossRef](#)]
37. Hong, H.C.; Krishnamurthy, C.B.; Borge-Durán, I.; Tasiar, M.; Gryko, D.T.; Grinberg, I.; Elbaz, L. Structural and Physical Parameters Controlling the Oxygen Reduction Reaction Selectivity with Carboxylic Acid-Substituted Cobalt Corroles Incorporated in a Porous Carbon Support. *J. Phys. Chem. C* **2019**, *123*, 26351–26357. [[CrossRef](#)]
38. Noffke, B.W.; Li, Q.; Raghavachari, K.; Li, L.-S. A Model for the pH-Dependent Selectivity of the Oxygen Reduction Reaction Electrocatalyzed by N-Doped Graphitic Carbon. *J. Am. Chem. Soc.* **2016**, *138*, 13923–13929. [[CrossRef](#)]
39. Sun, J.K.; Xu, Q. Functional materials derived from open framework templates/precursors: Synthesis and applications. *Energy Environ. Sci.* **2014**, *7*, 2071–2100. [[CrossRef](#)]
40. Han, X.P.; Ling, X.F.; Wang, Y.; Ma, T.Y.; Zhong, C.; Hu, W.B.; Deng, Y.D. Spatial Isolation of Zeolitic Imidazole Frameworks-Derived Cobalt Catalysts: From Nanoparticle, Atomic Cluster to Single Atom. *Angew. Chem. Int. Ed.* **2019**, *58*, 5359–5364. [[CrossRef](#)]
41. Yang, M.J.; Hu, X.H.; Fang, Z.S.; Sun, L.; Yuan, Z.K.; Wang, S.Y.; Hong, W.; Chen, X.D.; Yu, D.S. Bifunctional MOF-Derived Carbon Photonic Crystal Architectures for Advanced Zn–Air and Li–S Batteries: Highly Exposed Graphitic Nitrogen Matters. *Adv. Funct. Mater.* **2017**, *27*, 1701971. [[CrossRef](#)]
42. Lei, Y.J.; Wei, L.; Zhai, S.L.; Wang, Y.Q.; Karahan, H.E.; Chen, X.C.; Zhou, Z.; Wang, C.J.; Sui, X.; Chen, Y. Metal-free bifunctional carbon electrocatalysts derived from zeolitic imidazolate framework for efficient water splitting. *Mater. Chem. Front.* **2018**, *2*, 102–111. [[CrossRef](#)]
43. Fan, L.L.; Liu, P.F.; Yan, X.C.; Gu, L.; Yang, Z.Z.; Yang, H.G.; Qiu, S.L.; Yao, X.D. Atomically isolated nickel species anchored on graphitized carbon for efficient hydrogen evolution Electrocatalysis. *Nat. Commun.* **2016**, *7*, 10667. [[CrossRef](#)]
44. Sun, X.; Lu, L.; Zhu, Q.; Wu, C.; Yang, D.; Chen, C.; Han, B. MoP nanoparticles supported on indium-doped porous carbon: Outstanding catalysts for highly efficient CO<sub>2</sub> electroreduction. *Angew. Chem. Int. Ed.* **2018**, *57*, 2427–2431. [[CrossRef](#)]
45. Sun, Y.; Silvioli, L.; Sahraie, N.R.; Ju, W.; Li, J.; Zitolo, A.; Li, S.; Bagger, A.; Arnarson, L.; Wang, X.; et al. Strasser, Activity-selectivity trends in the electrochemical production of hydrogen peroxide over single-site metal-nitrogen-carbon catalysts. *J. Am. Chem. Soc.* **2019**, *141*, 12372–12381. [[CrossRef](#)]
46. Gao, J.; Yang, H.B.; Huang, X.; Hung, S.-F.; Cai, W.; Jia, C.; Miao, S.; Chen, H.M.; Yang, X.; Huang, Y.; et al. Enabling direct H<sub>2</sub>O<sub>2</sub> production in acidic media through rational design of transition metal single atom catalyst. *Chem* **2020**, *6*, 658–674. [[CrossRef](#)]
47. Wang, X.X.; Cullen, D.A.; Pan, Y.-T.; Hwang, S.; Wang, M.; Feng, Z.; Wang, J.; Engelhard, M.H.; Zhang, H.; He, Y.; et al. Nitrogen-coordinated single cobalt atom catalysts for oxygen reduction in proton exchange membrane fuel cells. *Adv. Mater.* **2018**, *30*, 1706758. [[CrossRef](#)]
48. He, Y.; Guo, H.; Hwang, S.; Yang, X.; He, Z.; Braaten, J.; Karakalos, S.; Shan, W.; Wang, M.; Zhou, H.; et al. Single cobalt sites dispersed in hierarchically porous nanofiber networks for durable and high-power PGM-free cathodes in fuel cells. *Adv. Mater.* **2020**, *32*, 2003577. [[CrossRef](#)]
49. Zhu, C.; Shi, Q.; Xu, B.Z.; Fu, S.; Wan, G.; Yang, C.; Yao, S.; Song, J.; Zhou, H.; Du, D.; et al. Hierarchically porous M–N–C (M = Co and Fe) single-atom electrocatalysts with robust M–Nx active moieties enable enhanced ORR performance. *Adv. Energy Mater.* **2018**, *8*, 1801956. [[CrossRef](#)]
50. Xie, X.; He, C.; Li, B.; He, Y.; Cullen, D.A.; Wegener, E.C.; Kropf, A.J.; Martinez, U.; Cheng, Y.; Engelhard, M.H.; et al. Performance enhancement and degradation mechanism identification of a single-atom Co–N–C catalyst for proton exchange membrane fuel cells. *Nat. Catal.* **2020**, *3*, 1044–1054. [[CrossRef](#)]
51. Liu, Y.M.; Quan, X.; Fan, X.F.; Wang, H.; Chen, S. High-Yield Electrosynthesis of Hydrogen Peroxide from Oxygen Reduction by Hierarchically Porous Carbon. *Angew. Chem. Int. Ed.* **2015**, *54*, 6837–6841. [[CrossRef](#)] [[PubMed](#)]
52. Zhang, D.Y.; Liu, T.C.; Yin, K.; Liu, C.B.; Wei, Y.F. Selective H<sub>2</sub>O<sub>2</sub> production on N-doped porous carbon from direct carbonization of metal organic frameworks for electro-Fenton mineralization of antibiotics. *Chem. Eng. J.* **2020**, *383*, 123184. [[CrossRef](#)]
53. Wang, D.; Feng, B.; Zhang, X.X.; Liu, Y.Y.; Pei, Y.; Qiao, M.H.; Zong, B.N. Nitrogen-doped Carbon Pyrolyzed from ZIF-8 for Electrocatalytic Oxygen Reduction to Hydrogen Peroxide. *Acta Chim. Sin.* **2022**, *80*, 772–780. [[CrossRef](#)]
54. Chang, J.L.; Wang, Y.F.; Chen, L.M.; Wu, D.P.; Xu, F.; Bai, Z.Y.; Jiang, K.; Gao, Z.Y. Cobalt nanoparticles embedded nitrogen doped carbon, preparation from alkali deprotonation assisted ZIF-67 and its electrocatalytic performance in oxygen evolution reaction. *Int. J. Hydrogen Energy* **2020**, *45*, 12787–12797. [[CrossRef](#)]
55. Shao, J.; Wan, Z.M.; Liu, H.M.; Zheng, H.Y.; Gao, T.; Shen, M.; Qu, Q.T.; Zheng, H.H. Metal organic frameworks-derived Co<sub>3</sub>O<sub>4</sub> hollow dodecahedrons with controllable interiors as outstanding anodes for Li storage. *J. Mater. Chem. A* **2014**, *2*, 12194–12200. [[CrossRef](#)]
56. Wu, Z.L.; Sun, L.P.; Yang, M.; Huo, L.H.; Zhao, H.; Grenier, J.C. Facile synthesis and excellent electrochemical performance of reduced graphene oxide–Co<sub>3</sub>O<sub>4</sub> yolk-shell nanocages as a catalyst for oxygen evolution reaction. *J. Mater. Chem. A* **2016**, *4*, 13534–13542. [[CrossRef](#)]

57. Asadi, F.; Azizi, S.N.; Ghasemi, S. A novel non-precious catalyst containing transition metal in nanoporous cobalt based metal-organic framework (ZIF-67) for electrooxidation of methanol. *J. Electroanal. Chem.* **2019**, *847*, 113181. [[CrossRef](#)]
58. Xuan, K.; Wan, J.; Gong, Z.H.; Wang, X.G.; Li, J.; Guo, Y.D.; Sun, Z.X. Hydroxyapatite modified ZIF-67 composite with abundant binding groups for the highly efficient and selective elimination of uranium (VI) from wastewater. *J. Hazard. Mater.* **2022**, *426*, 127834. [[CrossRef](#)]
59. Chen, S.C.; Chen, Z.H.; Siahrostami, S.; Kim, T.R.; Nordlund, D.; Sokaras, D.; Nowak, S.; To, J.W.F.; Higgins, D.; Sinclair, R.; et al. Defective Carbon-Based Materials for the Electrochemical Synthesis of Hydrogen Peroxide. *ACS Sustain. Chem. Eng.* **2018**, *6*, 311–317. [[CrossRef](#)]
60. Zhang, J.; Zhang, H.; Cheng, M.J.; Lu, Q. Tailoring the Electrochemical Production of H<sub>2</sub>O<sub>2</sub>: Strategies for the Rational Design of High-Performance Electrocatalysts. *Small* **2019**, *16*, 1902845. [[CrossRef](#)]
61. Roman, D.S.; Krishnamurthy, D.; Garg, R.; Hafiz, H.; Lamparski, M.; Nuhfer, N.T.; Meunier, V.; Viswanathan, V.; Cohen-karni, T. Engineering Three-Dimensional (3D) Out-of-Plane Graphene Edge Sites for Highly Selective Two-Electron Oxygen Reduction Electrocatalysis. *ACS Catal.* **2020**, *10*, 1993–2008. [[CrossRef](#)]
62. Wang, W.; Lu, X.Y.; Su, P.; Li, Y.W.; Cai, J.J.; Zhang, Q.Z.; Zhou, M.H.; Arotiba, O. Enhancement of hydrogen peroxide production by electrochemical reduction of oxygen on carbon nanotubes modified with fluorine. *Chemosphere* **2020**, *259*, 127423. [[CrossRef](#)]
63. Dong, K.; Liang, J.; Wang, Y.Y.; Xu, Z.Q.; Liu, Q.; Luo, Y.L.; Li, T.S.; Li, L.; Shi, X.F.; Asiri, A.M.; et al. Honeycomb Carbon Nanofibers: A Superhydrophilic O<sub>2</sub>-Entrapping Electrocatalyst Enables Ultrahigh Mass Activity for the Two-Electron Oxygen Reduction Reaction. *Angew. Chem. Int. Ed.* **2020**, *60*, 10583–10587. [[CrossRef](#)] [[PubMed](#)]
64. Xia, Y.; Zhao, X.H.; Xia, C.; Wu, Z.Y.; Zhu, P.; Kim (Timothy), J.Y.; Bai, X.W.; Gao, G.H.; Hu, Y.F.; Zhong, J.; et al. Highly active and selective oxygen reduction to H<sub>2</sub>O<sub>2</sub> on boron-doped carbon for high production rates. *Nat. Commun.* **2021**, *12*, 4225. [[CrossRef](#)] [[PubMed](#)]
65. Zhang, C.Y.; Liu, G.Z.; Ning, B.; Qian, S.R.; Zheng, D.N.; Wang, L. Highly efficient electrochemical generation of H<sub>2</sub>O<sub>2</sub> on N/O co-modified defective carbon. *Int. J. Hydrog. Energy* **2021**, *46*, 14277–14287. [[CrossRef](#)]
66. Han, L.; Yu, X.Y.; Lou, X.W. Formation of Prussian-Blue-Analog Nanocages via a Direct Etching Method and their Conversion into Ni-Co-Mixed Oxide for Enhanced Oxygen Evolution. *Adv. Mater.* **2016**, *28*, 4601–4605. [[CrossRef](#)]
67. McCrory, C.C.L.; Jung, S.; Peters, J.C.; Jaramillo, T.F. Benchmarking Heterogeneous Electrocatalysts for the Oxygen Evolution Reaction. *J. Am. Chem. Soc.* **2013**, *135*, 16977–16987. [[CrossRef](#)]
68. Wang, Z.; Li, Q.-K.; Zhang, C.; Cheng, Z.; Chen, W.; Mchugh, E.A.; Carter, R.A.; Jakobson, B.I.; Tour, J.M. Hydrogen Peroxide Generation with 100% Faradaic Efficiency on Metal-Free Carbon Black. *ACS Catal.* **2021**, *11*, 2454–2459.
69. Sun, Y.Y.; Li, S.; Paul, B.; Han, L.; Strasser, P. Highly efficient electrochemical production of hydrogen peroxide over nitrogen and phosphorus dual-doped carbon nanosheet in alkaline medium. *J. Electroanal. Chem.* **2021**, *896*, 115197. [[CrossRef](#)]
70. Lee, Y.H.; Li, F.; Chang, K.H.; Hu, C.C.; Ohsaka, T. Novel synthesis of N-doped porous carbons from collagen for electrocatalytic production of H<sub>2</sub>O<sub>2</sub>. *Appl. Catal. B* **2012**, *126*, 208–214. [[CrossRef](#)]
71. Chen, Z.; Chen, S.; Siahrostami, S.; Chakthranont, P.; Hahn, C.; Nordlund, D.; Dimosthenis, S.; Nørskov, J.K.; Bao, Z.; Jaramillo, T.F.; et al. Development of a reactor with carbon catalysts for modular-scale, low-cost electrochemical generation of H<sub>2</sub>O<sub>2</sub>. *Chem. Eng.* **2017**, *2*, 239–245. [[CrossRef](#)]
72. Lu, Z.Y.; Chen, G.X.; Siahrostami, S.Z.; Chen, H.; Liu, K.; Xie, J.; Liao, L.; Wu, T.; Lin, D.C.; Liu, Y.Y.; et al. High-efficiency oxygen reduction to hydrogen peroxide catalysed by oxidized carbon materials. *Nat. Catal.* **2018**, *1*, 156–162. [[CrossRef](#)]
73. Chen, S.; Chen, Z.; Siahrostami, S.; Higgins, D.; Nordlund, D.; Sokaras, D.; Kim, T.R.; Liu, Y.; Yan, X.; Nilsson, E.; et al. Designing Boron Nitride Islands in Carbon Materials for Efficient Electrochemical Synthesis of Hydrogen Peroxide. *J. Am. Chem. Soc.* **2018**, *140*, 7851–7859. [[CrossRef](#)] [[PubMed](#)]
74. Yang, W.L.; Zhou, M.H.; Cai, J.J.; Liang, L.; Ren, G.B.; Jiang, L.L. Ultrahigh yield of hydrogen peroxide on graphite felt cathode modified with electrochemically exfoliated graphene. *J. Mater. Chem. A* **2017**, *5*, 8070–8080. [[CrossRef](#)]
75. Chai, G.L.; Hou, Z.F.; Ikeda, T.; Terakura, K. Two-Electron Oxygen Reduction on Carbon Materials Catalysts: Mechanisms and Active Sites. *J. Phys. Chem. C* **2017**, *121*, 14524–14533. [[CrossRef](#)]
76. Su, H.; Gao, P.; Wang, M.Y.; Zhai, G.Y.; Zhang, J.J.; Zhao, T.J.; Su, J.; Antonietti, M.; Li, X.H.; Chen, J.S. Grouping effect of single Ni-N<sub>4</sub> sites in N-doped carbon boosts hydrogen transfer coupling of alcohols and amines. *Angew. Chem. Int. Ed.* **2018**, *57*, 15194–15198. [[CrossRef](#)]
77. Graham, D.J.; Nocera, D.G. Electrocatalytic H<sub>2</sub> Evolution by Proton-Gated Hangman Iron Porphyrins. *Organometallics* **2014**, *33*, 4994–5001. [[CrossRef](#)]
78. Chen, F.F.; Wang, N.; Lei, H.T.; Guo, D.Y.; Liu, H.F.; Zhang, Z.Y.; Zhang, W.; Lai, W.Z.; Cao, R. Electrocatalytic Water Oxidation by a Water-Soluble Copper (II) Complex with a Copper-Bound Carbonate Group Acting as a Potential Proton Shuttle. *Inorg. Chem.* **2017**, *56*, 13368–13375. [[CrossRef](#)]
79. Sun, H.L.; Han, Y.Z.; Lei, H.T.; Chen, M.X.; Cao, R. Cobalt corroles with phosphonic acid pendants as catalysts for oxygen and hydrogen evolution from neutral aqueous solution. *Chem. Commun.* **2017**, *53*, 6195–6198. [[CrossRef](#)]

80. Zhang, W.; Lai, W.Z.; Cao, R. Energy-Related Small Molecule Activation Reactions: Oxygen Reduction and Hydrogen and Oxygen Evolution Reactions Catalyzed by Porphyrin- and Corrole-Based Systems. *Chem. Rev.* **2017**, *117*, 3717–3797. [[CrossRef](#)]
81. Li, L.; Tang, C.; Zheng, Y.; Xia, B.Q.; Zhou, X.L.; Xu, H.L.; Qiao, S.Z. Tailoring Selectivity of Electrochemical Hydrogen Peroxide Generation by Tunable Pyrrolic-Nitrogen-Carbon. *Adv. Energy Mater.* **2020**, *10*, 852–863.

**Disclaimer/Publisher's Note:** The statements, opinions and data contained in all publications are solely those of the individual author(s) and contributor(s) and not of MDPI and/or the editor(s). MDPI and/or the editor(s) disclaim responsibility for any injury to people or property resulting from any ideas, methods, instructions or products referred to in the content.